

# Direct Partial Transformation of 2D Antimony Oxybromide to Halide Perovskite Heterostructure for Efficient CO<sub>2</sub> Photoreduction

Su-Xian Yuan, Ke Su, Meng-Ran Zhang, You-Xiang Feng, Yu Li,\* Min Zhang,\* and Tong-Bu Lu

The photocatalytic activity of lead-free perovskite heterostructures currently suffers from low efficiency due to the lack of active sites and the inadequate photogenerated carrier separation, the latter of which is hindered by slow charge transfer at the heterostructure interfaces. Herein, a facile strategy is reported for the construction of lead-free halide-perovskite-based heterostructure with swift interfacial charge transfer, achieved through direct partial conversion of 2D antimony oxybromide Sb<sub>4</sub>O<sub>5</sub>Br<sub>2</sub> to generate Cs<sub>3</sub>Sb<sub>2</sub>Br<sub>9</sub>/Sb<sub>4</sub>O<sub>5</sub>Br<sub>2</sub> heterostructure. Compared to the traditional electrostatic self-assembly method, this approach endows the Cs<sub>3</sub>Sb<sub>2</sub>Br<sub>9</sub>/Sb<sub>4</sub>O<sub>5</sub>Br<sub>2</sub> heterostructure with a tightly interconnected interface through in situ partial conversion, significantly accelerating interfacial charge transfer and thereby enhancing the separation efficiency of photogenerated carriers. The cobalt-doped Cs<sub>3</sub>Sb<sub>2</sub>Br<sub>9</sub>/Sb<sub>4</sub>O<sub>5</sub>Br<sub>2</sub> heterostructure demonstrates a record-high electron consumption rate of 840 μmol g<sup>-1</sup> h<sup>-1</sup> for photocatalytic CO<sub>2</sub> reduction to CO coupled with H<sub>2</sub>O oxidation to O<sub>2</sub>, which is over 74- and 16-fold higher than that of individual Sb<sub>4</sub>O<sub>5</sub>Br<sub>2</sub> and Cs<sub>3</sub>Sb<sub>2</sub>Br<sub>9</sub>, respectively. This work provides an effective strategy for promoting charge separation in photocatalysts to improve the performance of artificial photosynthesis.

#### 1. Introduction

Mimicking natural photosynthesis to convert  $\mathrm{CO}_2$  and  $\mathrm{H}_2\mathrm{O}$  into value-added chemicals with renewable solar energy is an appealing approach to mitigating the energy and climate issues due to the excessive combustion of fossil fuels. <sup>[1]</sup> In this technology, the light absorption efficiency and charge separation efficiency are pivotal in determining the performance of photocatalytic  $\mathrm{CO}_2$  reduction, <sup>[2]</sup> serving as the cornerstone for the development of

S.-X. Yuan, K. Su, M.-R. Zhang, Y.-X. Feng, Y. Li, M. Zhang, T.-B. Lu MOE International Joint Laboratory of Materials Microstructure Institute for New Energy Materials and Low Carbon Technologies School of Materials Science and Engineering

Tianjin University of Technology

Tianjin 300384, China

E-mail: yli@email.tjut.edu.cn; zm2016@email.tjut.edu.cn

The ORCID identification number(s) for the author(s) of this article can be found under https://doi.org/10.1002/smll.202409909

DOI: 10.1002/smll.202409909

diverse photocatalysts.[3] Consequently, halide perovskite materials, which have recently gained prominence in the optoelectronic device domains,[4] have garnered significant attention in the field of photocatalytic CO2 reduction,[5] owing to their desirable attributes, including outstanding visible light absorption capacity and prolonged carrier lifetime.<sup>[6]</sup> In particular, Sb-based perovskites exhibit reduced toxicity than Pb-based perovskites, while also demonstrating superior light absorption coefficients and extended carrier lifetimes compared to other lead-free halide perovskites (e.g., Sn-based, Bibased, AgBi-based, etc.).[7] Therefore, they are viewed as promising candidates for photocatalytic CO2 reduction.[8]

Nonetheless, akin to Pb-based perovskites, isolated Sb-based per-ovskite nanomaterials also encounter a shortage of high-activity sites. Furthermore, their nanosecond-scale photogenerated carrier lifetimes fall short of efficiently catalyzing the sluggish reactions of CO<sub>2</sub> reduction and water oxidation. Therefore, the

photocatalytic activity of standalone Sb-based perovskite nanomaterials for CO<sub>2</sub> reduction is also very low. Constructing ligandfree Sb-based perovskite nanomaterials has been demonstrated to be an effective solution to facilitate the exposure of active sites and strengthen CO2 adsorption, bringing forth enhanced performance for photocatalytic CO<sub>2</sub> reduction. [9] The charge separation efficiency can be enhanced by introducing mixed halides, which can not only tune the band gap of Sb-based perovskites, [10] but also promote favorable charge redistribution due to lower octahedral distortion, resulting in strengthened CO2 adsorption and activation.[11] Another widely adopted and proven effective approach to facilitating charge separation is the construction of heterostructures. For instance, depositing Sb-based perovskite onto Co<sub>3</sub>O<sub>4</sub> or Bi<sub>2</sub>MoO<sub>6</sub> can boost its charge separation, ultimately enhancing its photocatalytic performance.[12] However, the current primary methods for constructing Sb-based perovskite heterostructures encompass physical mixing and in situ deposition, and the resultant loose interfaces impede the process of interfacial charge transfer, ultimately constraining the efficient separation of photogenerated carriers. Therefore, the development of

16136829, 0, Downloaded from https://onlinelibrary.wiley.com/doi/10.1002/smll.202409909 by Tianjin University Of, Wiley Online Library on [03/02/2025]. See the Terms and Conditions (https://onlinelibrary.wiley.com/

and-conditions) on Wiley Online Library for rules of use; OA articles are governed by the applicable Creative Commons License

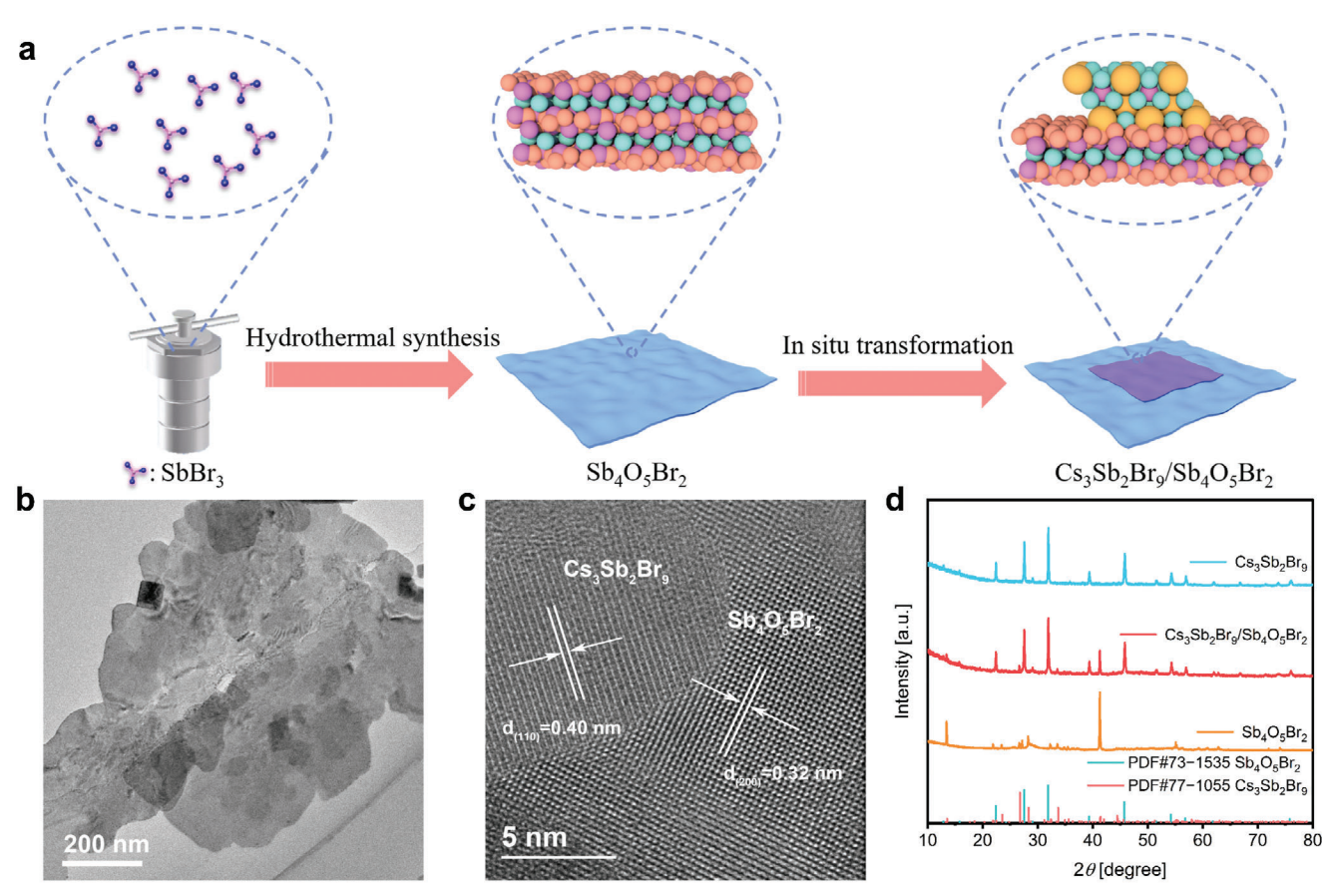


Figure 1. a) Schematic diagram of  $Cs_3Sb_2Br_9/Sb_4O_5Br_2$  preparation process. b,c) TEM and HRTEM images of  $Cs_3Sb_2Br_9/Sb_4O_5Br_2$ . d) XRD patterns of  $Cs_3Sb_2Br_9$ ,  $Sb_4O_5Br_2$  and  $Cs_3Sb_2Br_9/Sb_4O_5Br_2$ .

Sb-based perovskite heterostructures with tightly contacted interfaces is essential to enhance their performance for  ${\rm CO_2}$  photoreduction.

Herein, we reported a facile self-templating method for constructing Sb-based perovskite heterostructures with intimate interfacial contact. Specifically, for the first time, 2D Sb<sub>4</sub>O<sub>5</sub>Br<sub>2</sub> nanosheets were successfully synthesized via a hydrothermal method and employed as templates to generate 2D/2D Cs<sub>3</sub>Sb<sub>2</sub>Br<sub>9</sub>/Sb<sub>4</sub>O<sub>5</sub>Br<sub>2</sub> heterostructures through direct partial conversion. Our strategy primarily rests on the following crucial considerations. First, 2D nanosheets offer abundant active sites and shorter carrier transfer distances to the surface, facilitating the adsorption and activation of the reaction substrates.[13] Second, the large interface contact area of the 2D/2D heterostructure can promote interfacial charge transfer and separation.<sup>[14]</sup> Third, in situ direct conversion can form a tightly contacting interface, thereby accelerating interfacial charge transfer and separation. As anticipated, the prepared Cs<sub>3</sub>Sb<sub>2</sub>Br<sub>9</sub>/Sb<sub>4</sub>O<sub>5</sub>Br<sub>2</sub> heterostructure exhibits significantly improved interfacial photogenerated charrier separation compared to the heterostructure prepared by the traditional electrostatic self-assembly method. Through cobalt ion doping to enhance active sites, the fabricated Co@Cs<sub>3</sub>Sb<sub>2</sub>Br<sub>9</sub>/Sb<sub>4</sub>O<sub>5</sub>Br<sub>2</sub> heterostructure can attain an electron consumption rate of 840 µmol g<sup>-1</sup> h<sup>-1</sup> for photocatalytic CO<sub>2</sub> reduction to CO without the necessity of any organic sacrificial agents, surpassing the performances of other halide perovskite materials reported under comparable conditions (Table S1, Supporting Information).

#### 2. Results and Discussion

# 2.1. Preparation and Characterization of 2D/2D $Cs_3Sb_2Br_9/Sb_4O_5Br_2$ Heterostructures

The synthesis process of the Cs<sub>3</sub>Sb<sub>2</sub>Br<sub>9</sub>/Sb<sub>4</sub>O<sub>5</sub>Br<sub>2</sub> heterostructure is illustrated in Figure 1a, and detailed synthetic steps are described in the Experimental Section. Briefly, Sb<sub>4</sub>O<sub>5</sub>Br<sub>2</sub> nanosheets were first synthesized by a hydrothermal method and subsequently dispersed uniformly in a solution of isopropanol containing saturated CsBr. Under vigorous stirring, a certain amount of HBr was added to trigger the in situ transformation from Sb<sub>4</sub>O<sub>5</sub>Br<sub>2</sub> to Cs<sub>3</sub>Sb<sub>2</sub>Br<sub>9</sub>/Sb<sub>4</sub>O<sub>5</sub>Br<sub>2</sub>. During this process, HBr can effectively drive Sb<sup>3+</sup> and Br<sup>-</sup> ions to release from the lattice of Sb<sub>4</sub>O<sub>5</sub>Br<sub>2</sub> nanosheets to their surfaces, thereby enabling the in situ recrystallization with Cs<sup>+</sup> ions in the solution to form  $Cs_3Sb_2Br_9$  nanosheets  $(Sb_4O_5Br_2 + HBr + CsBr \rightarrow$  $Cs_3Sb_2Br_0 + H_2O$ ). Simultaneously, the proportion of the two components in the Cs<sub>3</sub>Sb<sub>2</sub>Br<sub>9</sub>/Sb<sub>4</sub>O<sub>5</sub>Br<sub>2</sub> heterostructure can also be effectively regulated by controlling the amount of HBr. For comparison, Cs<sub>3</sub>Sb<sub>2</sub>Br<sub>9</sub>:Sb<sub>4</sub>O<sub>5</sub>Br<sub>2</sub> composites were additionally

16136829, D. Downloaded from https://onlinelibrary.wiley.com/doi/10.1002/smll.102409999 by Tianjin University Of, Wiley Online Library on [03022025]. See the Terms and Conditions (https://onlinelibrary.wiley.com/rerms-and-conditions) on Wiley Online Library for rules of use; OA articles are governed by the applicable Creative Commons Licensean (1002) and (1002)

prepared by integrating  $Cs_3Sb_2Br_9$  and  $Sb_4O_5Br_2$  via the conventional electrostatic self-assembly method, with comprehensive details outlined in the Experimental Section.

The morphologies of the as prepared heterostructures were analyzed using transmission electron microscopy (TEM) and atomic force microscopy (AFM). As illustrated in Figure S1a (Supporting Information), TEM measurement revealed that the prepared Sb<sub>4</sub>O<sub>5</sub>Br<sub>2</sub> templates exhibit an irregular nanosheet morphology. The high-resolution TEM (HRTEM) image of Sb<sub>4</sub>O<sub>5</sub>Br<sub>2</sub> displays a lattice spacing of 0.32 nm, corresponding to the (200) plane of monoclinic Sb<sub>4</sub>O<sub>5</sub>Br<sub>2</sub> (Figure S1b, Supporting Information). Additionally, AFM measurement confirmed the nanosheet morphology of Sb<sub>4</sub>O<sub>5</sub>Br<sub>2</sub>, with an average thickness of approximately 10 nm (Figure S2, Supporting Information). Figure 1b displays the TEM image of the Cs<sub>3</sub>Sb<sub>2</sub>Br<sub>9</sub>/Sb<sub>4</sub>O<sub>5</sub>Br<sub>2</sub> heterostructure formed by in situ transformation, where it is clearly visible that small and darker nanosheets with a diameter of approximately 40 nm are distributed on the surface of the Sb<sub>4</sub>O<sub>5</sub>Br<sub>2</sub> nanosheets. Further, corresponding HRTEM measurements demonstrated two distinct lattice spacings of 0.32 and 0.40 nm, which can be attributed to the (200) plane of Sb<sub>4</sub>O<sub>5</sub>Br<sub>2</sub> and the (110) plane of Cs<sub>3</sub>Sb<sub>2</sub>Br<sub>9</sub>, respectively (Figure 1c). These lattice spacings are consistent with those of pure Sb<sub>4</sub>O<sub>5</sub>Br<sub>2</sub> and Cs<sub>3</sub>Sb<sub>2</sub>Br<sub>9</sub>, as shown in Figures S1,S3 (Supporting Information), respectively. Energy-dispersive X-ray spectroscopy (EDS) mapping measurements were further conducted to investigate the elemental distribution in the Cs<sub>3</sub>Sb<sub>2</sub>Br<sub>9</sub>/Sb<sub>4</sub>O<sub>5</sub>Br<sub>2</sub> heterostructure. As depicted in Figure S4 (Supporting Information), Sb and O are uniformly dispersed throughout the sample, while Cs and Br are relatively concentrated. The above results provide preliminary evidence for the successful preparation of the Cs<sub>3</sub>Sb<sub>2</sub>Br<sub>9</sub>/Sb<sub>4</sub>O<sub>5</sub>Br<sub>2</sub> heterostructure.

Powder X-ray diffraction (PXRD) measurements were conducted to delve deeper into the crystal structure characteristics of the Cs<sub>3</sub>Sb<sub>2</sub>Br<sub>9</sub>/Sb<sub>4</sub>O<sub>5</sub>Br<sub>2</sub> heterostructure. As presented in Figure 1d, the as-prepared Sb<sub>4</sub>O<sub>5</sub>Br<sub>2</sub> nanosheets exhibit sharp diffraction peaks, indicating high crystallinity. These diffraction peaks are situated at 13.5°, 21.9°, 27.3°, 28.4°, and 41.4°, corresponding to the (100), (012), (200), (–104) and (300) planes of the monoclinic phase Sb<sub>4</sub>O<sub>5</sub>Br<sub>2</sub> (JCPDS No. 73–1535). After undergoing in situ partial conversion, the characteristic diffraction peaks of Sb<sub>4</sub>O<sub>5</sub>Br<sub>2</sub> are still observable in the sample. More notably, the emergence of characteristic diffraction peaks corresponding to the highly crystalline hexagonal phase Cs<sub>3</sub>Sb<sub>2</sub>Br<sub>9</sub> (JCPDS No. 77–1055) provides compelling evidence for the successful preparation of the Cs<sub>3</sub>Sb<sub>2</sub>Br<sub>9</sub>/Sb<sub>4</sub>O<sub>5</sub>Br<sub>2</sub> heterostructure. [15]

Fourier transform infrared (FTIR) spectroscopy and Raman spectroscopy measurements further confirmed the successful preparation of the  $Cs_3Sb_2Br_9/Sb_4O_5Br_2$  composites. As shown in Figure S5 (Supporting Information),  $Sb_4O_5Br_2$  exhibits a prominent vibration peak of Sb–O–Sb at 826 cm $^{-1}$ , with characteristic peaks at 703 and 494 cm $^{-1}$  attributed to the stretching and bending vibrations of the Sb–O bond, respectively.  $^{[16]}$  In contrast,  $Cs_3Sb_2Br_9$ , due to its inherent ionic crystalline nature, does not exhibit significant characteristic signals in the FTIR spectrum. Notably, in the  $Cs_3Sb_2Br_9/Sb_4O_5Br_2$  heterostructure, the aforementioned characteristic peaks of  $Sb_4O_5Br_2$  can be distinctly detected, which strongly supports the notion that the compos-

ite is constructed through partial conversion using  $Sb_4O_5Br_2$  as the substrate. Moreover, the Raman signals can be unequivocally observed belonging to  $Cs_3Sb_2Br_9$  (72, 183, and 213 cm<sup>-1</sup> corresponding to  $E_g$  and  $A_{1g}$  modes)<sup>[17]</sup> and  $Sb_4O_5Br_2$  (104, 124, and 170 cm<sup>-1</sup> are observed to the external Sb–Br stretching pattern of  $A_{1g}$  and  $E_g$ . The peak observed at 261 cm<sup>-1</sup> is from the vibration of O–Sb–O, and the 461 cm<sup>-1</sup> band generated by oxygen atoms motion is  $B_{1g}$ )<sup>[18]</sup> in  $Cs_3Sb_2Br_9/Sb_4O_5Br_2$  heterostructure (Figure S6, Supporting Information). These results collectively demonstrate the successful preparation of the  $Cs_3Sb_2Br_9/Sb_4O_5Br_2$  heterostructure.

## 2.2. Interfacial Charge Transfer Dynamics of Cs<sub>3</sub>Sb<sub>2</sub>Br<sub>9</sub>/Sb<sub>4</sub>O<sub>5</sub>Br<sub>2</sub> Heterostructures

The UV-visible diffuse reflectance spectroscopy (UV-vis DRS) and ultraviolet photoelectron spectroscopy (UPS) measurements were employed to assess the thermodynamic feasibility of the composites for the photocatalytic CO<sub>2</sub> reduction. As depicted in Figure 2a, Sb<sub>4</sub>O<sub>5</sub>Br<sub>2</sub> exhibits relatively weak absorption in the visible light region, with an absorption edge at only 411 nm. In contrast, Cs<sub>3</sub>Sb<sub>2</sub>Br<sub>9</sub> demonstrates superior light absorption capability in the UV-vis region below 501 nm. Notably, the characteristic absorption features of both Sb<sub>4</sub>O<sub>5</sub>Br<sub>2</sub> and Cs<sub>3</sub>Sb<sub>2</sub>Br<sub>9</sub> can be observed in the  $Cs_3Sb_2Br_9/Sb_4O_5Br_2$  heterostructure, further confirming the successful synthesis of the composite material. According to the corresponding Tauc plots (Figure S7, Supporting Information), the optical band gaps of Cs<sub>3</sub>Sb<sub>2</sub>Br<sub>9</sub> and Sb<sub>4</sub>O<sub>5</sub>Br<sub>2</sub> can be determined to be 2.54 and 2.67 eV, respectively, which are consistent with previous reports.<sup>[19]</sup> Figures 2b and c display the UPS spectra of Cs<sub>3</sub>Sb<sub>2</sub>Br<sub>9</sub> and Sb<sub>4</sub>O<sub>5</sub>Br<sub>2</sub>, respectively. From these spectra, the valence band edge potentials  $(E_{VB})$  of  $Cs_3Sb_2Br_9$  and  $Sb_4O_5Br_2$  are calculated to be 2.08 and 2.02 V versus the standard hydrogen electrode (SHE), respectively. By combining the values of  $E_{\rm g}$  and  $E_{\rm VB}$ , the conduction band edge potentials ( $E_{CB}$ ) of  $Cs_3Sb_2Br_9$  and  $Sb_4O_5Br_2$  can be inferred to be -0.46 and -0.65 V versus SHE, respectively. In addition, Mott-Schottky measurements were conducted to determine the flat-band potentials of Cs<sub>3</sub>Sb<sub>2</sub>Br<sub>9</sub> and Sb<sub>4</sub>O<sub>5</sub>Br<sub>2</sub>, which were found to be -0.46 and -0.65 V versus SHE, respectively, aligning with the UPS measurement results (Figure S8, Supporting Information). Notably, staggered energy band alignments exist in the Cs<sub>3</sub>Sb<sub>2</sub>Br<sub>9</sub>/Sb<sub>4</sub>O<sub>5</sub>Br<sub>2</sub> composite, which is advantageous for the separation and transfer of photogenerated carriers. Furthermore, the migration direction of photogenerated carriers in the Cs<sub>3</sub>Sb<sub>2</sub>Br<sub>9</sub>/Sb<sub>4</sub>O<sub>5</sub>Br<sub>2</sub> heterostructure during the photocatalytic process was investigated by the in situ photo-excited high-resolution X-ray photoelectron spectroscopy (XPS). As presented in Figures 2d and e, under illumination, the binding energy of O 1s in Cs<sub>3</sub>Sb<sub>2</sub>Br<sub>9</sub>/Sb<sub>4</sub>O<sub>5</sub>Br<sub>2</sub> shifts toward higher binding energy (0.22–0.49 eV), while the binding energy of Cs 3d shifts toward lower binding energy (0.41 eV). These changes indicate that light irradiation causes the electron densities of around the Cs and O atoms to increase and decrease, respectively, signifying that the photogenerated carriers undergo directional transfer at the heterojunction interface. Specifically, photogenerated electrons transfer from Sb<sub>4</sub>O<sub>5</sub>Br<sub>2</sub> to Cs<sub>3</sub>Sb<sub>2</sub>Br<sub>9</sub>, while photogenerated holes transfer in the opposite direction. The band structure

16136389, D. Downloaded from https://onlinelibrary.wiley.com/doi/10.1002/smll.202409999 by Tianjin University Of, Wiley Online Library on [03.022025]. See the Terms and Conditions (https://onlinelibrary.wiley.com/rerms-and-conditions) on Wiley Online Library for rules of use; OA articles are governed by the applicable Creative Commons Licensea

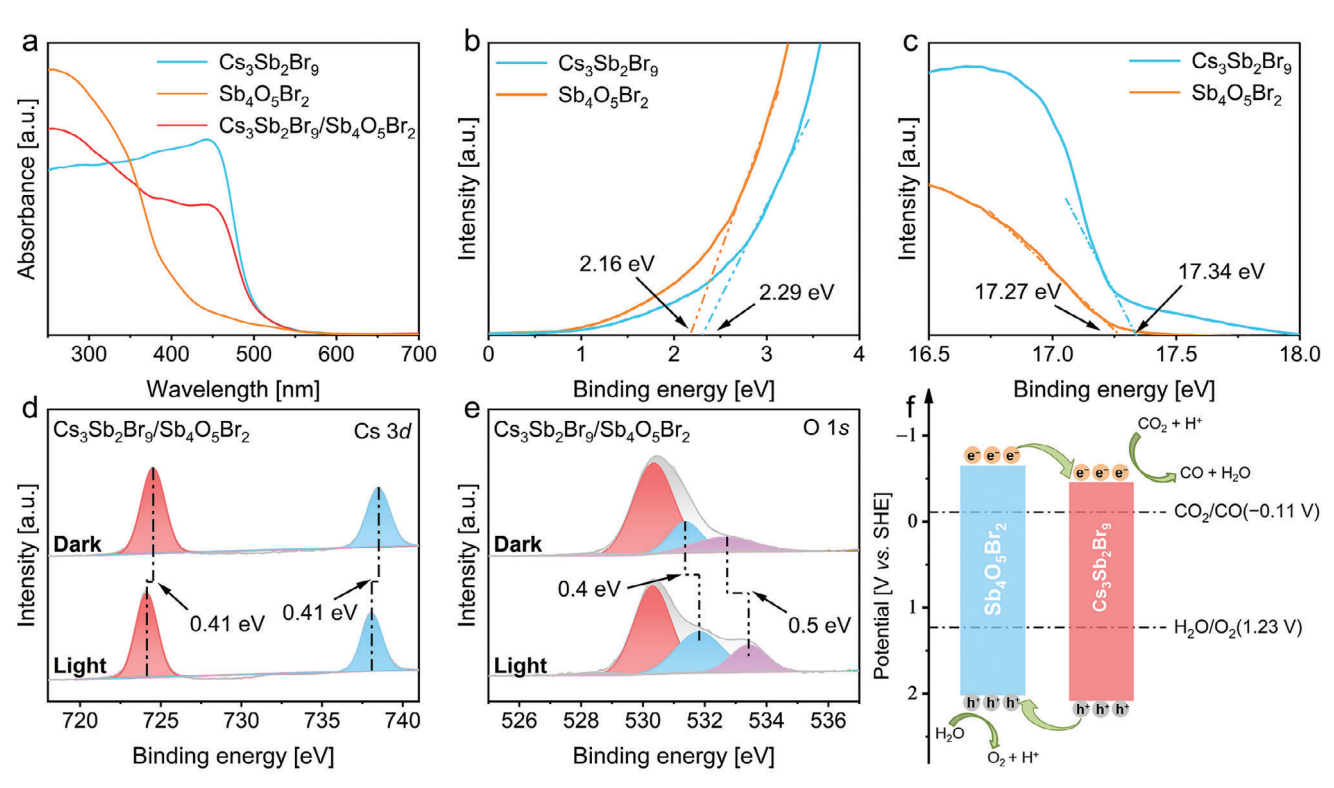


Figure 2. a) UV-vis DRS spectra of  $Cs_3Sb_2Br_9$ ,  $Sb_4O_5Br_2$ , and  $Cs_3Sb_2Br_9$ / $Sb_4O_5Br_2$ . b,c) UPS spectra of  $Cs_3Sb_2Br_9$  and  $Sb_4O_5Br_2$ . In situ high-resolution XPS spectra of  $Cs_3Sb_2Br_9$ / $Sb_4O_5Br_2$  under the light and dark conditions: d)  $Cs_3d$  and e)  $Cs_3Sb_2Br_9$  and  $Cs_3Sb_2Br_9$ 

and electron transfer direction of the Cs<sub>3</sub>Sb<sub>2</sub>Br<sub>9</sub>/Sb<sub>4</sub>O<sub>5</sub>Br<sub>2</sub> heterostructure are schematically illustrated in Figure 2f.

The dynamics of photogenerated carriers in photocatalysts is a crucial factor determining their photocatalytic performance.<sup>[20]</sup> Therefore, the dynamics of photogenerated carriers in the Cs<sub>3</sub>Sb<sub>2</sub>Br<sub>9</sub>/Sb<sub>4</sub>O<sub>5</sub>Br<sub>2</sub> heterostructure were further investigated through steady-state and transient photoluminescence (PL) measurements. The excitation wavelength of 420 nm was chosen to avoid the absorption of Sb<sub>4</sub>O<sub>5</sub>Br<sub>2</sub>. As depicted in Figure 3a, pure Cs<sub>3</sub>Sb<sub>2</sub>Br<sub>9</sub> exhibits strong PL emission with a characteristic peak at 490 nm. There is an insignificant reduced PL intensity in the Cs<sub>3</sub>Sb<sub>2</sub>Br<sub>9</sub>:Sb<sub>4</sub>O<sub>5</sub>Br<sub>2</sub> composite based on the electrostatic self-assembly method, indicating the sluggish electron transfer between Cs<sub>3</sub>Sb<sub>2</sub>Br<sub>9</sub> and Sb<sub>4</sub>O<sub>5</sub>Br<sub>2</sub> because of the structural separation of the two components. It is worth noting that the Cs<sub>3</sub>Sb<sub>2</sub>Br<sub>9</sub>/Sb<sub>4</sub>O<sub>5</sub>Br<sub>2</sub> heterostructure exhibits dramatic PL quenching, indicating that the high-quality interface is beneficial for the separation of photogenerated carriers. The timeresolved PL (TRPL) measurements further confirmed that the heterostructure formed by in situ conversion promotes interfacial charge separation, as shown in Figure 3b. The TRPL decay curve of pure Cs<sub>3</sub>Sb<sub>2</sub>Br<sub>9</sub> represents both radiative and nonradiative pathways of photogenerated excitons in Cs<sub>3</sub>Sb<sub>2</sub>Br<sub>9</sub>. The average PL lifetime of Cs<sub>3</sub>Sb<sub>2</sub>Br<sub>9</sub> can be calculated by fitting the corresponding TRPL decay curve with a multi-exponential function, resulting in a value of 3.30 ns (Table S2, Supporting Information). In comparison to Cs<sub>3</sub>Sb<sub>2</sub>Br<sub>9</sub>, the Cs<sub>3</sub>Sb<sub>2</sub>Br<sub>9</sub>:Sb<sub>4</sub>O<sub>5</sub>Br<sub>7</sub> composite exhibits accelerated PL decay with a shorter average PL lifetime of 2.07 ns, further indicating that interfacial charge transfer occurs between Cs<sub>3</sub>Sb<sub>2</sub>Br<sub>9</sub> and Sb<sub>4</sub>O<sub>5</sub>Br<sub>2</sub>. In contrast, the PL decay in the Cs<sub>3</sub>Sb<sub>2</sub>Br<sub>9</sub>/Sb<sub>4</sub>O<sub>5</sub>Br<sub>2</sub> heterostructure is significantly accelerated, and the average lifetime is shortened to 1.37 ns, indicating that the rapid charge transfer at the interface of the Cs<sub>3</sub>Sb<sub>2</sub>Br<sub>9</sub>/Sb<sub>4</sub>O<sub>5</sub>Br<sub>2</sub> heterostructure. These results also confirm that the closely contacting interface is highly beneficial for the separation of photogenerated charge carriers. Photocurrent response (I-t) and electrochemical impedance spectroscopy (EIS) measurements further demonstrated the advantage of the in situ transformation strategy for accelerating interfacial charge transport and separation. As shown in Figure 3c, the photocurrent densities of the Cs<sub>3</sub>Sb<sub>2</sub>Br<sub>9</sub>/Sb<sub>4</sub>O<sub>5</sub>Br<sub>2</sub> were apparently higher than those of single Cs<sub>3</sub>Sb<sub>2</sub>Br<sub>9</sub>, Sb<sub>4</sub>O<sub>5</sub>Br<sub>2</sub> and the Cs<sub>3</sub>Sb<sub>2</sub>Br<sub>9</sub>:Sb<sub>4</sub>O<sub>5</sub>Br<sub>2</sub> heterostructure formed by electrostatic self-assembly. In addition, the diameter of the Nyquist semicircle of the Cs<sub>3</sub>Sb<sub>2</sub>Br<sub>9</sub>/Sb<sub>4</sub>O<sub>5</sub>Br<sub>2</sub> heterostructure is also significantly smaller than that of the Cs<sub>3</sub>Sb<sub>2</sub>Br<sub>9</sub>, Sb<sub>4</sub>O<sub>5</sub>Br<sub>2</sub> and Cs<sub>3</sub>Sb<sub>2</sub>Br<sub>9</sub>:Sb<sub>4</sub>O<sub>5</sub>Br<sub>2</sub>, respectively (Figure S9, Supporting Information).

The surface photovoltage (SPV) measurements were further carried out to confirm the favorable effects of the heterostructure formed by in situ conversion strategy on photogenerated carrier transport and separation. The AFM height mapping images reveal that both the pristine Sb<sub>4</sub>O<sub>5</sub>Br<sub>2</sub> and the transformed Cs<sub>3</sub>Sb<sub>2</sub>Br<sub>9</sub>/Sb<sub>4</sub>O<sub>5</sub>Br<sub>2</sub> exhibit a nanosheet morphology. The Kelvin probe force microscopy (KPFM) images (Figures S10,S11, Supporting Information) and the SPV difference are shown in Figure 3d. Under illumination, the larger change in the SPV signal typically indicates more accumulation

16136829, D. Downloaded from https://onlinelibrary.wiley.com/doi/10.1002/smll.102409999 by Tianjin University Of, Wiley Online Library on [03022025]. See the Terms and Conditions (https://onlinelibrary.wiley.com/rerms-and-conditions) on Wiley Online Library for rules of use; OA articles are governed by the applicable Creative Commons Licensean (1002) and (1002)

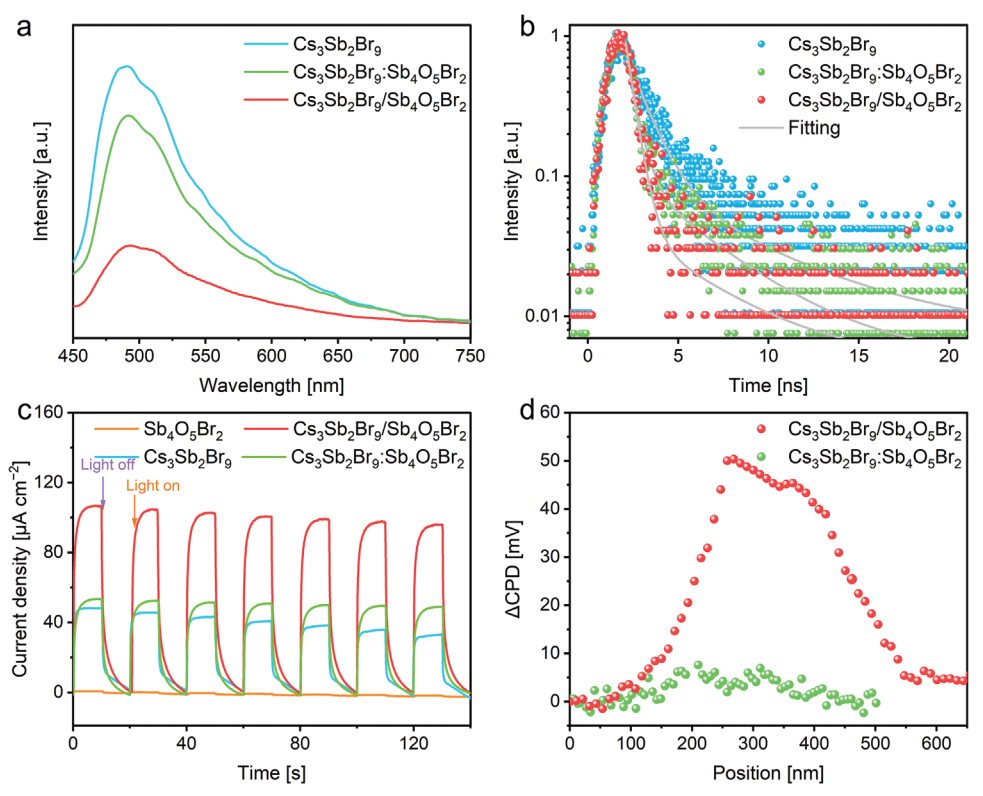


Figure 3. a) Steady-state PL and b) time-resolved PL decay traces of Cs<sub>3</sub>Sb<sub>2</sub>Br<sub>9</sub>, Cs<sub>3</sub>Sb<sub>2</sub>Br<sub>9</sub>;Sb<sub>4</sub>O<sub>5</sub>Br<sub>2</sub> and Cs<sub>3</sub>Sb<sub>2</sub>Br<sub>9</sub>/Sb<sub>4</sub>O<sub>5</sub>Br<sub>2</sub>. c) I-t curves of  $Cs_3Sb_2Br_9$ ,  $Sb_4O_5Br_2$ ,  $Cs_3Sb_2Br_9$ : $Sb_4O_5Br_2$ , and  $Cs_3Sb_2Br_9/Sb_4O_5Br_2$ . d) Surface potential changes of  $Cs_3Sb_2Br_9$ : $Sb_4O_5Br_2$  and  $Cs_3Sb_2Br_9/Sb_4O_5Br_2$ . by subtracting the potential under dark conditions from that under illumination.

of photogenerated charge on the surface of semiconductor. Pure Sb<sub>4</sub>O<sub>5</sub>Br<sub>2</sub> has a negligible SPV response under light irradiation, due to the rapid charge carrier recombination and the weak light absorption capacity (Figure \$12, Supporting Information). In addition, the SPV response of pure Cs<sub>3</sub>Sb<sub>2</sub>Br<sub>9</sub> is correspondingly negligible (Figure S13, Supporting Information). Notably, as shown in Figure 3d, Cs<sub>3</sub>Sb<sub>2</sub>Br<sub>9</sub>/Sb<sub>4</sub>O<sub>5</sub>Br<sub>2</sub> shows an obvious change of SPV signals, which is also substantially larger than that of Cs<sub>3</sub>Sb<sub>2</sub>Br<sub>9</sub>:Sb<sub>4</sub>O<sub>5</sub>Br<sub>2</sub> composite. Apparently, the Cs<sub>3</sub>Sb<sub>2</sub>Br<sub>9</sub>/Sb<sub>4</sub>O<sub>5</sub>Br<sub>2</sub> heterostructure with a close contact interface can promote interfacial charge separation, resulting in a high concentration of photogenerated charge carriers at the semiconductor surface. The significant difference in SPV signals furnishes strong evidence for the accumulation and consumption of space charge on the interface of the Cs<sub>3</sub>Sb<sub>2</sub>Br<sub>9</sub>/Sb<sub>4</sub>O<sub>5</sub>Br<sub>2</sub> heterostructure interface.

#### 2.3. Photocatalytic CO<sub>2</sub> Reduction Activity and Mechanism of Cs<sub>3</sub>Sb<sub>2</sub>Br<sub>9</sub>/Sb<sub>4</sub>O<sub>5</sub>Br<sub>2</sub> Heterostructures

The photocatalytic CO2 reduction activities of all the prepared samples were evaluated using a gas-solid reaction system with the presence of H<sub>2</sub>O vapor. A 300 W Xe lamp with a light intensity of 100 mW cm<sup>-2</sup> was used to simulate sunlight. The gaseous products were analyzed by gas chromatography, and neither CH4 nor H2 were detected, revealing that CO was the primary product of CO<sub>2</sub> reduction for all the evaluated samples (Figure \$14, Supporting Information). The corresponding CO generation rates of all photocatalysts are shown in Figure 4a. The Sb<sub>4</sub>O<sub>5</sub>Br<sub>2</sub> nanosheets exhibit very inferior activity for photocatalytic CO2 reduction with a CO production rate of 6 µmol g<sup>-1</sup> h<sup>-1</sup>. This is attributed to their weak light absorption capacity and weak thermodynamic driving force for the reduction reaction. Meanwhile, individual Cs<sub>3</sub>Sb<sub>2</sub>Br<sub>9</sub> also displays low activity for photocatalytic  $CO_2$  reduction (26  $\mu$ mol  $g^{-1}$   $h^{-1}$ ), despite its ideal light absorption and energy band structure, primarily due to its deficiency active sites and insufficient photogenerated carriers. Compared with Cs<sub>3</sub>Sb<sub>2</sub>Br<sub>9</sub> and Sb<sub>4</sub>O<sub>5</sub>Br<sub>2</sub>, the CO<sub>2</sub> reduction capacity of the Cs<sub>3</sub>Sb<sub>2</sub>Br<sub>9</sub>:Sb<sub>4</sub>O<sub>5</sub>Br<sub>2</sub> catalyst formed by electrostatic self-assembly was slightly improved with a CO generation rate of 41 µmol g<sup>-1</sup> h<sup>-1</sup>. This result should be attributed to the large distance between the two composites formed by electrostatic self-assembly, which hinders the charge transfer and leads to insufficient photogenerated carrier separation. For Cs<sub>3</sub>Sb<sub>2</sub>Br<sub>9</sub>/Sb<sub>4</sub>O<sub>5</sub>Br<sub>2</sub>, the proportion of Cs<sub>3</sub>Sb<sub>2</sub>Br<sub>9</sub> and Sb<sub>4</sub>O<sub>5</sub>Br<sub>2</sub> was optimized via controlling the HBr volume (Figure \$15, Supporting Information). Notably, the optimal Cs<sub>3</sub>Sb<sub>2</sub>Br<sub>9</sub>/Sb<sub>4</sub>O<sub>5</sub>Br<sub>2</sub> delivered significantly improved photocatalytic CO2 reduction activity, and the CO yield is as high as 202  $\mu$ mol g<sup>-1</sup> h<sup>-1</sup>, which suggests that the close-contact heterostructure interface is conducive to improving the photogenerated carrier separation efficiency. Moreover, considering that incorporating active metal ions into halide perovskites can enhance the catalytic activity for CO2 reduction by increasing catalytic site and improving charge separation

16136829, D. Downloaded from https://onlinelibrary.wiley.com/doi/10.1002/smll.102409999 by Tianjin University Of, Wiley Online Library on [03022025]. See the Terms and Conditions (https://onlinelibrary.wiley.com/rerms-and-conditions) on Wiley Online Library for rules of use; OA articles are governed by the applicable Creative Commons Licensean (1002) and (1002)

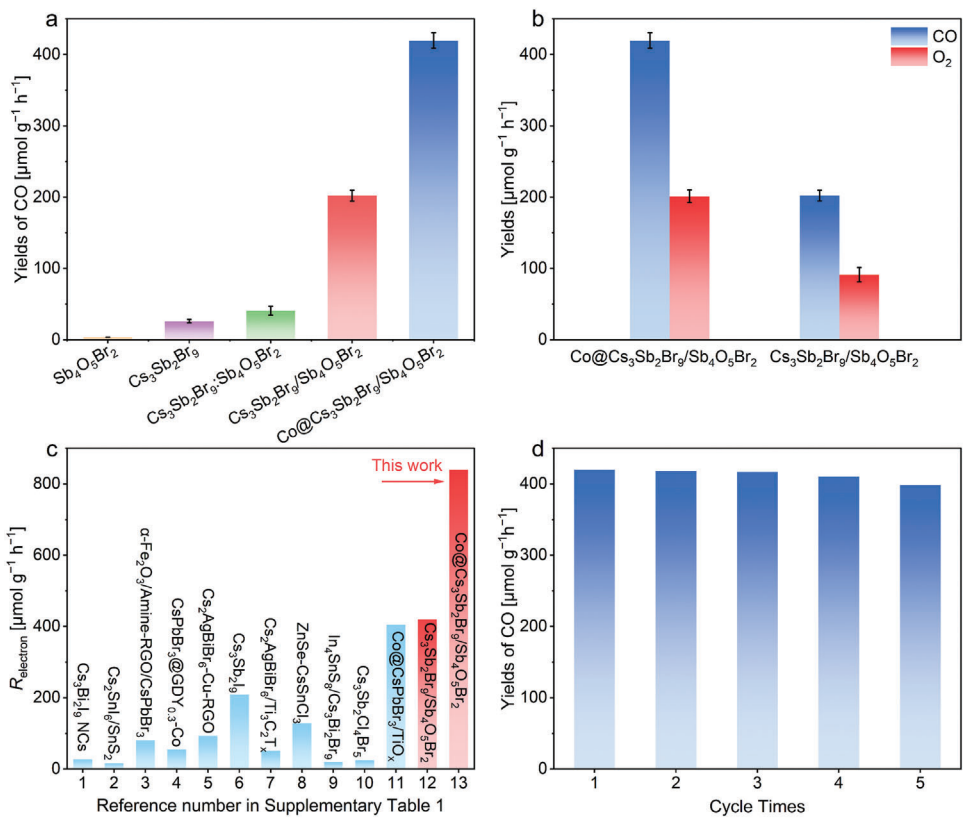


Figure 4. a) Yields of CO with different catalysts. b) Yields of reduced and oxidized products with Co@Cs<sub>3</sub>Sb<sub>2</sub>Br<sub>9</sub>/Sb<sub>4</sub>O<sub>5</sub>Br<sub>2</sub> and Cs<sub>3</sub>Sb<sub>2</sub>Br<sub>9</sub>/Sb<sub>4</sub>O<sub>5</sub>Br<sub>2</sub> as photocatalysts. c) Comparison of electron consumption rates of reported halide perovskite-based photocatalysts. d) Yields of CO for consecutive five cycles with 2 h each using Co@Cs<sub>3</sub>Sb<sub>2</sub>Br<sub>9</sub>/Sb<sub>4</sub>O<sub>5</sub>Br<sub>2</sub> as photocatalyst.

efficiency, a cobalt doped Cs<sub>3</sub>Sb<sub>2</sub>Br<sub>9</sub>/Sb<sub>4</sub>O<sub>5</sub>Br<sub>2</sub> heterostructure, designated as Co@Cs<sub>3</sub>Sb<sub>2</sub>Br<sub>9</sub>/Sb<sub>4</sub>O<sub>5</sub>Br<sub>2</sub>, was also synthesized (Figures S16–S18, Supporting Information). The CO formation rate of Co@Cs<sub>3</sub>Sb<sub>2</sub>Br<sub>9</sub>/Sb<sub>4</sub>O<sub>5</sub>Br<sub>2</sub> could reach up to 420 µmol g<sup>-1</sup> h<sup>−1</sup>, which is more than an order of magnitude higher than that of Cs<sub>3</sub>Sb<sub>2</sub>Br<sub>9</sub> and Sb<sub>4</sub>O<sub>5</sub>Br<sub>2</sub> and Cs<sub>3</sub>Sb<sub>2</sub>Br<sub>9</sub>:Sb<sub>4</sub>O<sub>5</sub>Br<sub>2</sub> composites alone (Figure 4a and Figure S19, Supporting Information). Meanwhile, the oxidation products O<sub>2</sub> of Co@Cs<sub>3</sub>Sb<sub>2</sub>Br<sub>9</sub>/Sb<sub>4</sub>O<sub>5</sub>Br<sub>2</sub> and Cs<sub>3</sub>Sb<sub>2</sub>Br<sub>9</sub>/Sb<sub>4</sub>O<sub>5</sub>Br<sub>2</sub> were quantified, averaging 202 and 91 µmol g<sup>-1</sup> h<sup>-1</sup>, respectively, maintaining a nearly stoichiometric of 1:2 ratio with respect to the yield of CO (Figure 4b). The corresponding electron consumption rate  $(R_{electron})$  of Co@Cs<sub>3</sub>Sb<sub>2</sub>Br<sub>9</sub>/Sb<sub>4</sub>O<sub>5</sub>Br<sub>2</sub> can reach up to 840 µmol g<sup>-1</sup> h<sup>-1</sup>, which is much higher than that of reported halideperovskite-based photocatalysts, as shown in Figure 4c. The apparent quantum efficiencies (AQEs) for Cs<sub>3</sub>Sb<sub>2</sub>Br<sub>9</sub>:Sb<sub>4</sub>O<sub>5</sub>Br<sub>2</sub>,  $Cs_3Sb_2Br_9/Sb_4O_5Br_9$  and  $Co@Cs_3Sb_2Br_9/Sb_4O_5Br_2$  were evaluated under 365 and 425 nm incident light (Table \$3, Supporting Information). The Cs<sub>3</sub>Sb<sub>2</sub>Br<sub>6</sub>:Sb<sub>4</sub>O<sub>5</sub>Br<sub>2</sub> only displays low AQE values of 0.02% and 0.01% under 365 and 425 nm LEDs, respectively. In sharp contrast, Cs<sub>3</sub>Sb<sub>2</sub>Br<sub>9</sub>/Sb<sub>4</sub>O<sub>5</sub>Br<sub>2</sub> delivered significantly higher AQE values of 0.11% and 0.08% under identical conditions, suggesting the facilitated charge transfer benefitting from the direct partial conversion strategy. Moreover, the AQE values of Co@Cs<sub>3</sub>Sb<sub>2</sub>Br<sub>9</sub>/Sb<sub>4</sub>O<sub>5</sub>Br<sub>2</sub> were further increased, demonstrating improved photon conversion after cobalt doping.

In addition, the photocatalytic stability of Cs<sub>3</sub>Sb<sub>2</sub>Br<sub>9</sub>/Sb<sub>4</sub>O<sub>5</sub>Br<sub>2</sub> and Co@Cs<sub>3</sub>Sb<sub>2</sub>Br<sub>9</sub>/Sb<sub>4</sub>O<sub>5</sub>Br<sub>2</sub> were estimated by cyclic experiments. As shown in Figure 4d and Figure S20 (Supporting Information), the CO generation rate decreased by less than 10% after 5 cycles, indicating that Cs<sub>3</sub>Sb<sub>2</sub>Br<sub>9</sub>/Sb<sub>4</sub>O<sub>5</sub>Br<sub>2</sub> and Co@Cs<sub>3</sub>Sb<sub>2</sub>Br<sub>9</sub>/Sb<sub>4</sub>O<sub>5</sub>Br<sub>2</sub> have good stability in the gassolid reaction system. Further, XRD and XPS measurements confirmed that the crystal structure and chemical state of Cs<sub>3</sub>Sb<sub>2</sub>Br<sub>9</sub>/Sb<sub>4</sub>O<sub>5</sub>Br<sub>2</sub> remained well after the photocatalytic reaction (Figures S21,S22, Supporting Information).

Using Cs<sub>3</sub>Sb<sub>2</sub>Br<sub>9</sub>/Sb<sub>4</sub>O<sub>5</sub>Br<sub>2</sub> as photocatalyst, further controlled experiments were conducted to determine the sources of CO and O<sub>2</sub>. As shown in Figure S23 (Supporting Information), no products were detected in the absence of light or catalyst, indicating that the CO<sub>2</sub> reduction reaction was triggered by light irradiation on the catalyst. In addition, a control experiment that was conducted in the absence of water vapor or with the replacement of CO<sub>2</sub> with Ar also demonstrated negligible generation of CO, indicating that CO originates from CO<sub>2</sub> photoreduction and the electron source for this photoreduction comes from water oxidation. Furthermore, the origins of the products were further verified by isotopic labeling experiments with <sup>13</sup>CO<sub>2</sub> and H<sub>2</sub><sup>18</sup>O as feedstocks. As presented in Figure S24 (Supporting Information), the results of mass spectrometry analysis from the <sup>13</sup>CO<sub>2</sub> isotope tracing experiment reveal an obvious signal at m/z =29, which belongs to <sup>13</sup>CO, proving that the CO originates from

16136829, 0, Downloaded from https://onlinelibrary.wiley.com/doi/10.1002/smll.202409909 by Tianjin University Of, Wiley Online Library on [03.02/2025]. See the Terms and Conditions (https://onlinelibrary.wiley.com/error

conditions) on Wiley Online Library for rules of use; OA articles are governed by the applicable Creative Commons License

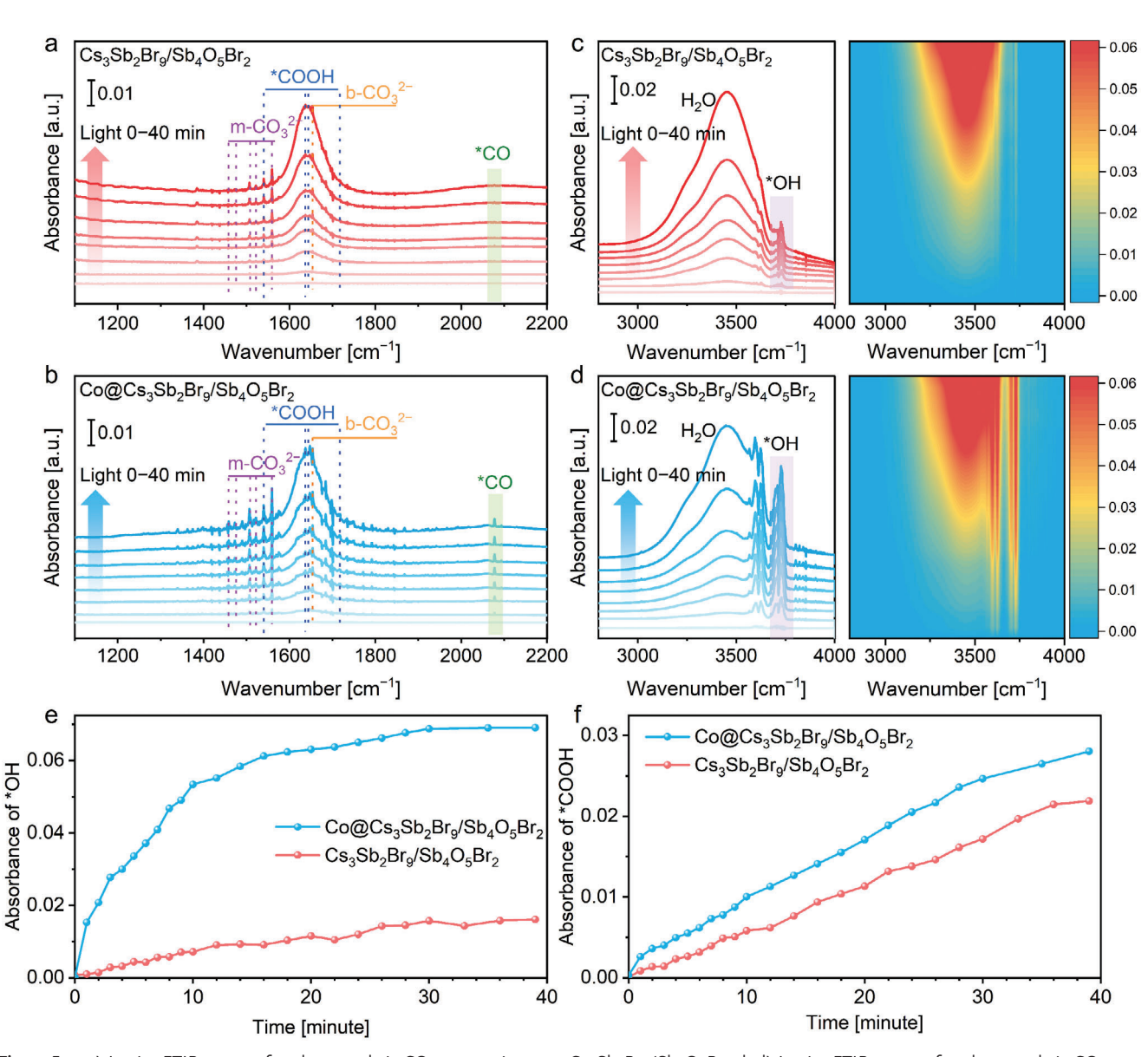


**Figure 5.** a,c) In situ FTIR spectra for photocatalytic CO $_2$  conversion over Cs $_3$ Sb $_2$ Br $_9$ /Sb $_4$ O $_5$ Br $_2$ . b,d) In situ FTIR spectra for photocatalytic CO $_2$  conversion over Co $_3$ Cs $_3$ Sb $_2$ Br $_9$ /Sb $_4$ O $_5$ Br $_2$ . e) Plots of time against adsorption strength in the \*COOH adsorption mode in in situ FTIR spectra. f) Plots of time against adsorption strength in the water stretching mode in in situ FTIR spectra.

 ${\rm CO_2}$  photoreduction. Additionally, in the  ${\rm H_2}^{18}{\rm O}$  isotope tracing experiment, the obvious signal at m/z=36 corresponding to  $^{18}{\rm O_2}$  can be detected, confirming that  ${\rm O_2}$  was derived from water oxidation. [21]

The role of doped cobalt in steering the dynamics of photogenerated charge carriers was also investigated. As shown in Figure S25 (Supporting Information), the PL intensity of  $Co@Cs_3Sb_2Br_9/Sb_4O_5Br_2$  drastically decreased in comparison with that for  $Cs_3Sb_2Br_9/Sb_4O_5Br_2$ , indicating the improved separation of photogenerated carriers by doped Co ions. In addition, the PL decay in the  $Co@Cs_3Sb_2Br_9/Sb_4O_5Br_2$  was accelerated, and the average lifetime was shortened from 1.37 to 0.84 ns, suggesting the facilitated charge transfer (Figure S26 and Table S2, Supporting Information). The favored charge

carrier separation and migration by cobalt doping were further validated by the higher photocurrent densities and smaller Nyquist semicircle of  $\text{Co@Cs}_3\text{Sb}_2\text{Br}_9/\text{Sb}_4\text{O}_5\text{Br}_2$  compared to those of  $\text{Cs}_3\text{Sb}_2\text{Br}_9/\text{Sb}_4\text{O}_5\text{Br}_2$  (Figures S27,S28, Supporting Information).

Furthermore, the adsorption and activation mechanisms of  $CO_2$  and  $H_2O$  during the photoconversion process were analyzed using in situ FTIR measurement. The measurements were conducted under equilibrium adsorption of  $CO_2$ -containing water vapor. As illustrated in **Figure 5a**,b, with the increase in illumination time, the emergence of new characteristic peaks of 1618, 1636, 1647, and 1716 cm<sup>-1</sup> were observed for both  $Cs_3Sb_2Br_9/Sb_4O_5Br_2$  and  $Co@Cs_3Sb_2Br_9/Sb_4O_5Br_2$ . These peaks were assigned to the \*COOH group, [20] which is

16136829, D. Downloaded from https://onlinelibrary.wiley.com/doi/10.1002/smll.102409999 by Tianjin University Of, Wiley Online Library on [03022025]. See the Terms and Conditions (https://onlinelibrary.wiley.com/rerms-and-conditions) on Wiley Online Library for rules of use; OA articles are governed by the applicable Creative Commons Licensean (1002) and (1002)

generally considered to be important intermediates in the CO2 reduction process.<sup>[22]</sup> In addition, the peaks at 1317, 1458, 1473, 1507, 1549 and 1559 cm<sup>-1</sup> can be attributed to monodentate carbonate (m-CO<sub>2</sub><sup>2-</sup>), while the bidentate carbonate (b-CO<sub>2</sub><sup>2-</sup>) peaks were observed at 1363 and 1653 cm<sup>-1</sup>. The observation of infrared peaks at 1696 cm<sup>-1</sup> was attributed to the \*CO.[23] Comparatively, for Co@Cs<sub>3</sub>Sb<sub>2</sub>Br<sub>9</sub>/Sb<sub>4</sub>O<sub>5</sub>Br<sub>2</sub>, the intensity of characteristic peaks (\*COOH and \*CO) was significantly higher, indicating that Co doping is conducive to the formation of \*COOH and \*CO (Figure 5b). The peak at 3200-3800 cm<sup>-1</sup> is assigned to adsorbed H<sub>2</sub>O molecules, [24] confirming that H<sub>2</sub>O molecules are involved in the CO2 reduction process, and the intensity of these peaks is commonly used to represent the ability of water activation.<sup>[25]</sup> The peak at 3300 cm<sup>-1</sup> is associated with the stretching vibration of hydroxyl groups, typically indicating physically adsorbed H<sub>2</sub>O molecules. The characteristic peak in the range of 3500-3800 cm<sup>-1</sup> generally represents the interaction between metal and hydroxyl groups (Sb-OH). [26] In contrast, the metal hydroxyl peak of the Co@Cs<sub>3</sub>Sb<sub>2</sub>Br<sub>9</sub>/Sb<sub>4</sub>O<sub>5</sub>Br<sub>2</sub> composite within the wavenumber range of 3700-3727 cm<sup>-1</sup> demonstrates a significant enhancement effect, which robustly indicates a substantial improvement in its water activation capability (as shown in Figure 5c,d). Furthermore, a meticulous analysis of the trend in \*OH signal intensity over time reveals that in the Cs<sub>3</sub>Sb<sub>2</sub>Br<sub>9</sub>/Sb<sub>4</sub>O<sub>5</sub>Br<sub>2</sub> system, the Sb-OH content gradually and steadily increases to an equilibrium state within the 0 to 40 min period. Concurrently, the Sb-OH on the surface of Co@Cs<sub>3</sub>Sb<sub>2</sub>Br<sub>9</sub>/Sb<sub>4</sub>O<sub>5</sub>Br<sub>2</sub> rapidly accumulates to its equilibrium level within the initial 10 min, and its Sb-OH concentration at equilibrium is over 3.5 times higher compared to that of the Cs<sub>3</sub>Sb<sub>2</sub>Br<sub>9</sub>/Sb<sub>4</sub>O<sub>5</sub>Br<sub>2</sub> material. Additionally, the evolution rate of the \*COOH intermediate on Co@Cs<sub>3</sub>Sb<sub>2</sub>Br<sub>9</sub>/Sb<sub>4</sub>O<sub>5</sub>Br<sub>2</sub> is faster than that based on Cs<sub>3</sub>Sb<sub>2</sub>Br<sub>9</sub>/Sb<sub>4</sub>O<sub>5</sub>Br<sub>2</sub>. This result clearly demonstrates that the incorporation of Co significantly promotes the water activation process, optimizes the carrier separation efficiency of the heterojunction, and thereby contributes to enhancing the CO<sub>2</sub> reduction efficiency (as shown in Figure 5e,f). Furthermore, the linear sweep voltammetry (LSV) curves for CO<sub>2</sub> reduction and oxygen evolution reaction (OER) provide additional evidence that cobalt doping facilitates both CO<sub>2</sub> reduction and H<sub>2</sub>O oxidation (Figures S29,S30, Supporting Information), which is consistent with the results obtained from in situ infrared spectroscopy.

Based on these results, we can propose the reaction pathway of Cs<sub>3</sub>Sb<sub>2</sub>Br<sub>9</sub>/Sb<sub>4</sub>O<sub>5</sub>Br<sub>2</sub> photocatalytic CO<sub>2</sub> reduction coupled with water oxidation. As illustrated in Figure \$31 (Supporting Information), first, Cs<sub>3</sub>Sb<sub>2</sub>Br<sub>9</sub>/Sb<sub>4</sub>O<sub>5</sub>Br<sub>2</sub> absorbs photons and produces electron-hole pairs. Subsequently, effective charge separation occurs for the photogenerated carriers, with electrons flowing toward Cs<sub>3</sub>Sb<sub>2</sub>Br<sub>9</sub> and holes accumulating in Sb<sub>4</sub>O<sub>5</sub>Br<sub>2</sub>. Following this, the photogenerated electrons in the conduction band of Cs<sub>3</sub>Sb<sub>2</sub>Br<sub>9</sub> initiate the reduction reaction of CO<sub>2</sub> through a proton-coupled electron transfer pathway, forming intermediates such as \*COOH and \*CO during the process. These intermediates then undergo further proton-coupled electron transfer reactions to produce CO. Simultaneously, the photogenerated holes in the valence band of Sb<sub>4</sub>O<sub>5</sub>Br<sub>2</sub> engage in the oxidation of H<sub>2</sub>O to \*OH intermediates, ultimately leading to the production  $O_2$ .

#### 3. Conclusion

In summary, two 2D/2D lead-free halide-perovskite-based heterostructures of Sb<sub>4</sub>O<sub>5</sub>Br<sub>2</sub>/Sb<sub>4</sub>O<sub>5</sub>Br<sub>2</sub> and Co@Cs<sub>3</sub>Sb<sub>2</sub>Br<sub>9</sub>/ Sb<sub>4</sub>O<sub>5</sub>Br<sub>2</sub> have been successfully prepared by combining selftemplating method with direct partial conversion approach and served as photocatalysts for CO<sub>2</sub> reduction coupled with water oxidation. This in situ partial transformation technology results in the formation of a tightly interconnected interface between Cs<sub>3</sub>Sb<sub>2</sub>Br<sub>9</sub> and Sb<sub>4</sub>O<sub>5</sub>Br<sub>2</sub>, which can accelerate interfacial photogenerated carrier separation, as demonstrated by a combination of steady-state and transient photoluminescence, photocurrent response, EIS and SPV measurements. Furthermore, in situ FTIR and LSV measurements revealed that doping cobalt ions can facilitate both CO2 reduction and H2O oxidation. Consequently, the prepared Co@Cs<sub>3</sub>Sb<sub>2</sub>Br<sub>9</sub>/Sb<sub>4</sub>O<sub>5</sub>Br<sub>2</sub> heterostructure achieves excellent performance for photocatalytic CO2 reduction, achieving a record-high electron consumption rate of 840  $\mu$ mol g<sup>-1</sup> h<sup>-1</sup>, which significantly surpasses that of other halide perovskite-based materials under similar conditions. The proposed direct partial transformation strategy opens up a new avenue to enhance spatial photogenerated carrier separation in halide perovskite-based heterostructures, and this approach could potentially be extended to the development of other heterostructure photocatalysts.

#### 4. Experimental Section

Preparation of Sb<sub>4</sub>O<sub>5</sub>Br<sub>2</sub> Nanosheets: Sb<sub>4</sub>O<sub>5</sub>Br<sub>2</sub> nanosheets were synthesized by the solvothermal synthesis method. First, 0.25 mmol of SbBr<sub>3</sub> (90.37 mg) and 9 mL of ethanol were added into a beaker and completely dissolved using ultrasound. The mixture was then stirred for 30 min. Next, 0.25 mmol of KBr was dispersed in 1 mL of deionized water and added dropwise to the above solution. After stirring for an additional 30 min, the mixture was transferred to a Teflon-line autoclave (25 mL) and maintained at 120 °C for 24 h. After cooling to room temperature, the mixture was washed with deionized water and ethanol and then dried at 60 °C

Preparation of Cs<sub>3</sub>Sb<sub>2</sub>Br<sub>9</sub>/Sb<sub>4</sub>O<sub>5</sub>Br<sub>2</sub> Heterostructures: First, 5 mg of Sb<sub>4</sub>O<sub>5</sub>Br<sub>2</sub> and 2 mL of isopropyl alcohol solution were added into a 5 mL flask. The compound was ultrasonicated for 30 min to ensure thorough dispersion. A methanol solution of CsBr (20 mg mL<sup>-1</sup>) was then added to the mixture under vigorous stirring and kept stirring for an additional 10 min. An isopropyl alcohol solution of HBr (V:V = 10:1) was injected into the mixture and kept stirring for another 5 min. Finally, the mixture was centrifuged at 5000 rpm for 3 min.

Preparation of Cs<sub>3</sub>Sb<sub>2</sub>Br<sub>9</sub> Nanocrystals: Cs<sub>3</sub>Sb<sub>2</sub>Br<sub>9</sub> nanocrystals were synthesized by the antisolvent precipitation method. First, the precursor solution of Cs<sub>3</sub>Sb<sub>2</sub>Br<sub>9</sub> was prepared by mixing 76 mg of CsBr, 86 mg of  $SbBr_2$  and 3 mL of dimethyl sulfoxide solution in a 10 mL glass vial. After complete dissolution, a 0.4 M Cs<sub>3</sub>Sb<sub>2</sub>Br<sub>9</sub> precursor solution was obtained. Then, 300 μL Cs<sub>3</sub> Sb<sub>2</sub> Br<sub>9</sub> precursor solution was added dropwise to 3 mL of isopropyl alcohol under vigorous stirring, resulting in a rapid color change to yellowish green. After stirring for 5 min, the mixture was centrifuged at 7000 rpm for 3 min. The obtained suspension was washed with isopropyl alcohol, and the precipitation was dried in a vacuum oven at 60 °C for

Preparation of Cs<sub>3</sub>Sb<sub>2</sub>Br<sub>9</sub>:Sb<sub>4</sub>O<sub>5</sub>Br<sub>2</sub> Heterostructures: First, 5 mg of Sb<sub>4</sub>O<sub>5</sub>Br<sub>2</sub> and 5 mg of Cs<sub>3</sub>Sb<sub>2</sub>Br<sub>9</sub> were dispersed in 2 mL of isopropyl alcohol, and then ultrasonicated for 30 min to ensure thorough dispersion. The mixture was stirred for 2 h afterward. After stirring, the mixture was centrifuged at 7000 rpm for 3 min, and the precipitates were dried in a vacuum oven at 60 °C.

\_ SMQ

16136829, D. Downloaded from https://onlinelibrary.wiley.com/doi/10.1002/smll.102409999 by Tianjin University Of, Wiley Online Library on [03022025]. See the Terms and Conditions (https://onlinelibrary.wiley.com/rerms-and-conditions) on Wiley Online Library for rules of use; OA articles are governed by the applicable Creative Commons Licensean (1002) and (1002)

Preparation of  $Co@Cs_3Sb_2Br_9/Sb_4O_5Br_2$  Heterostructures: The synthesis process of  $Co@Cs_3Sb_2Br_9/Sb_4O_5Br_2$  was similar to that of  $Cs_3Sb_2Br_9/Sb_4O_5Br_2$ , except that an adding methanol solution CsBr and  $CoBr_2$  (0.05 M) was added to replace pure CsBr methanol solution in the initial step.

### **Supporting Information**

Supporting Information is available from the Wiley Online Library or from the author.

## Acknowledgements

This work was financially supported by the National Key R&D Program of China (2022YFA1502902), the NSFC (22475152, U21A20286 and 21931007) and the 111 Project of China.

#### **Conflict of Interest**

The authors declare no conflict of interest.

#### **Data Availability Statement**

The data that support the findings of this study are available from the corresponding author upon reasonable request.

#### **Keywords**

carrier separation,  ${\rm CO}_2$  reduction, heterostructure, lead-free halide perovskite, photocatalysis

Received: October 23, 2024 Revised: December 30, 2024 Published online:

- [1] a) W. Gao, S. Liang, R. Wang, Q. Jiang, Y. Zhang, Q. Zheng, B. Xie, C. Y. Toe, X. Zhu, J. Wang, L. Huang, Y. Gao, Z. Wang, C. Jo, Q. Wang, L. Wang, Y. Liu, B. Louis, J. Scott, A. Roger, R. Amal, H. He, S. Park, Chem. Soc. Rev. 2020, 49, 8584; b) T. A. Jacobson, J. S. Kler, M. T. Hernke, R. K. Braun, K. C. Meyer, W. E. Funk, Nat. Sustain. 2019, 2, 691
- [2] a) S. Fang, M. Rahaman, J. Bharti, E. Reisner, M. Robert, G. A. O., Y. Hu, Nat. Rev. Methods Primers 2023, 3, 61; b) O. S. Bushuyev, P. D. Luna, C. T. Dinh, L. Tao, G. Saur, J. Lagemaat, S. O. Kelley, E. H. Sargent, Joule 2018, 2, 825; c) G. Lan, Y. Fan, W. Shi, E. You, S. S. Veroneau, W. Lin, Nat. Catal. 2022, 5, 1006; d) M. Bonchio, J. Bonin, O. Ishitani, T.-B. Lu, T. Morikawa, A. J. Morris, E. Reisner, D. Sarkar, F. M. Toma, M. Robert, Nat. Catal. 2023, 6, 657.
- [3] a) W. Soontornchaiyakul, S. Yoshino, T. Kanazawa, R. Haruki, D. Fan, S. Nozawa, Y. Yamaguchi, A. Kudo, J. Am. Chem. Soc. 2023, 145, 20485; b) Z. Jiang, X. Xu, Y. Ma, H. S. Cho, D. Ding, C. Wang, J. Wu, P. Oleynikov, M. Jia, J. Cheng, Y. Zhou, O. Terasaki, T. Peng, L. Zan, H. Deng, Nature 2020, 586, 549; c) Q.-S. Huang, Y. Zhang, P. Liu, H. Yang, X. Zhang, S.-H. Wei, Proc. Natl. Acad. Sci. USA 2024, 121, 2318341121; d) Q. Geng, L. Fan, H. Chen, C. Zhang, Z. Xu, Y. Tian, C. Yu, L. Kang, Y. Yamauchi, C. Li, L. Jiang, J. Am. Chem. Soc. 2024, 15, 10599; e) T. Han, X. Cao, H.-C. Chen, J. Ma, Y. Yu, Y. Li, W. Xu, K. Sun, A. Huang, Z. Chen, C. Chen, H. Zhang, B. Ye, Q. Peng, Y. Li, Angew. Chem., Int. Ed. 2023, 62, 202313325. f) Z.-K. Xin, Y.-J. Gao, Y. Gao, H.-W. Song, J. Zhao, F. Fan, A.-D. Xia, X.-B. Li, C.-H. Tung, L.-Z. Wu, Adv. Mater. 2022, 34, 2106662.

- [4] a) N. P. Gallop, D. R. Maslennikov, N. Mondal, K. P. Goetz, Z. Dai, A. M. Schankler, W. Sung, S. Nihonyanagi, T. Tahara, M. I. Bodnarchuk, M. V. Kovalenko, Y. Vaynzof, A. M. Rappe, A. A. Bakulin, Nat. Mater. 2024, 23, 88; b) S. E. Ng, N. Yantara, N. A. Tu, E. Erdenebileg, P. W. F. Li, D. Sharma, Y. M. Lam, S. Mhaisalkar, A. Basu, A. Chattopadhyay, N. Mathews, Adv. Mater. 2024, 36, 2406568; c) M. V. Kovalenko, L. Protesescu, M. I. Bodnarchuk, Science 2017, 358, 745; d) Y. Hassan, J. H. Park, M. L. Crawford, A. Sadhanala, J. Lee, J. C. Sadighian, E. Mosconi, R. Shivanna, E. Radicchi, M. Jeong, C. Yang, H. Choi, S. H. Park, M. H. Song, F. D. Angelis, C. Y. Wong, R. H. Friend, B. R. Lee, H. J. Snaith, Nature 2021, 591, 72.
- [5] a) Y.-F. Xu, M.-Z. Yang, B.-X. Chen, X.-D. Wang, H.-Y. Chen, D.-B. Kuang, C.-Y. Su, J. Am. Chem. Soc. 2017, 139, 5660; b) M. Ou, W. Tu, S. Yin, W. Xing, S. Wu, H. Wang, S. Wan, Q. Zhong, R. Xu, Angew. Chem., Int. Ed. 2018, 57, 13570; c) K. Su, S.-X. Yuan, L.-Y. Wu, Z.-L. Liu, M. Zhang, T.-B. Lu, Small 2023, 19, 2301192; d) W. Song, K. C. Chong, G. Qi, Y. Xiao, G. Chen, B. Li, Y. Tang, X. Zhang, Y. Yao, Z. Lin, Z. Zou, B. Liu, J. Am. Chem. Soc. 2024, 146, 3303.
- [6] a) X.-K. Liu, W. Xu, S. Bai, Y. Jin, J. Wang, R. H. Friend, F. Gao, Nat. Mater. 2021, 20, 10; b) Z.-Y. Chen, N.-Y. Huang, Q. Xu, Coord. Chem. Rev. 2023, 481, 215031.
- [7] a) M. Chen, K. Chang, Y. Zhang, Z. Zhang, Y. Dong, X. Qiu, H. Jiang, Y. Zhu, J. Zhu, Angew. Chem., Int. Ed. 2023, 62, 202305530; b) Z. Chen, X. Jiang, H. Xu, J. Wang, M. Zhang, D. Pan, G. Jiang, M. Z. Shahid, Z. Li, Small 2024, 20, 2401202; c) Y.-X. Feng, K. Su, Z.-L. Liu, S.-X. Yuan, Y.-F. Mu, M. Zhang, T.-B. Lu, Appl. Catal. B Environ. Energy 2024, 347, 123821; d) R. Cheng, Z.-B. Liang, L. Zhu, H. Li, Y. Zhang, C.-F. Wang, S. Chen, Angew. Chem., Int. Ed. 2022, 61, 202204371.
- [8] a) J.-S. Zhao, Y.-F. Mu, L.-Y. Wu, Z.-M. Luo, L. Velasco, M. Sauvan, D. Moonshiram, J.-W. Wang, M. Zhang, T.-B. Lu, *Angew. Chem., Int. Ed.* 2024, 63, 202401344; b) J. Zhu, Y. Zhang, Z. Chen, Z. Zhang, X. Tian, M. Huang, X. Bai, X. Wang, Y. Zhu, H. Jiang, *Nat. Commun.* 2024, 15, 1565.
- [9] a) Y.-F. Mu, J.-S. Zhao, L.-Y. Wu, K.-Y. Tao, Z.-L. Liu, F.-Q. Bai, D.-C. Zhong, M. Zhang, T.-B. Lu, Appl. Catal. B Environ. 2023, 338, 123024;
  b) Y. Wang, Q. Zhou, Y. Zhu, D. Xu, Appl. Catal. B Environ. 2021, 294, 120236
- [10] D. Wu, B. Huo, Y. Huang, X. Zhao, J. Yang, K. Hu, X. Mao, P. He, Q. Huang, X. Tang, Small 2022, 18, 2106001.
- [11] J. Lee, W.-K. Chong, S. H. W. Kok, B.-J. Ng, X. Y. Kong, S.-P. Chai, L.-L. Tan, Adv. Funct. Mater. 2023, 33, 2303430.
- [12] a) T. Shan, S. Ke, X. Yang, X. Yang, B. Weng, L. Shen, M.-Q. Yang, Appl. Catal. B Environ. Energy 2025, 361, 124602; b) S. Wongthep, P. Pluengphon, D. Tantraviwat, W. Panchan, S. Boochakiat, K. Jarusuphakornkul, Q. Wu, J. Chen, B. Inceesungvorn, J. Colloid Interface Sci. 2024, 655, 32.
- [13] a) J. Wang, Z. Li, H. Chen, G. Deng, X. Niu, Nano-Micro Lett. 2019, 11, 48; b) E. Yamamoto, D. Kurimoto, K. Ito, K. Hayashi, M. Kobayashi, M. Osadam, Nat. Commun. 2024, 15, 6612.
- [14] a) A. Sood, J. B. Haber, J. Carlström, E. A. Peterson, E. Barre, J. D. Georgaras, A. H. M. Reid, X. Shen, M. E. Zajac, E. C. Regan, J. Yang, T. Taniguchi, K. Watanabe, F. Wang, X. Wang, J. B. Neaton, T. F. Heinz, A. M. Lindenberg, F. H. da Jornada, A. Raja, Nat. Nanotech. 2023, 18, 29; b) S.-X. Yuan, K. Su, Y.-X. Feng, M. Zhang, T.-B. Lu, Chin. Chem. Lett. 2023, 34, 107682.
- [15] H.-H. Zhang, Z.-C. Zhou, Y.-J. Dong, L. Zhang, H.-Y. Chen, D.-B. Kuang, Sol. RRL 2021, 5, 2100559.
- [16] S. Paul, B. Sen, N. Chakraborty, S. Das, S. Mondal, A. P. Chattopadhyaya, S. I. Ali, RSC Adv. 2022, 12, 8374.
- [17] P. Liu, Y. Liu, S. Zhang, J. Li, C. Wang, C. Zhao, P. Nie, Y. Dong, X. Zhang, S. Zhao, G. Wei, Adv. Optical Mater. 2020, 8, 2001072.
- [18] a) Y. Shi, D. Zhou, T. Wu, Z. Xiao, ACS Appl. Mater. Interfaces 2022, 14, 29905; b) E. Jiang, L. Yang, N. Song, X. Zhang, C. Liu, H. Dong, J. Colloid Interf. Sci. 2020, 576, 21; c) K. Ramakrishnan, C. Nithya, B. K.

16136829, 0, Downloaded from https://onlinelibrary.wiley.com/doi/10.1002/smll.202409909 by Tianjin University Of, Wiley Online Library on [03.02/2025]. See the Terms

and Conditions (https://onlinelibrary.wiley.com/terms-and-conditions) on Wiley Online Library for rules

of use; OA articles are governed by the applicable Creative Commons License

- Purushothaman, N. Kumar, S. Gopukumar, ACS Sustainable Chem. Eng. 2017, 5, 5090.
- [19] Z. Zhang, Y. Yang, Y. Wang, L. Yang, Q. Li, L. Chen, D. Xu, Angew. Chem., Int. Ed. 2020, 59, 18136.
- [20] a) H. Li, C. Cheng, Z. Yang, J. Wei, Nat. Commun. 2022, 13, 6466; b) P. Zhou, I. A. Navid, Y. Ma, Y. Xiao, P. Wang, Z. Ye, B. Zhou, K. Sun, Z. Mi, Nature 2023, 613, 66.
- [21] W. Wang, C. Deng, S. Xie, Y. Li, W. Zhang, H. Sheng, C. Chen, J. Zhao, J. Am. Chem. Soc. 2021, 143, 2984.
- [22] a) L. Liang, X. Li, Y. Sun, Y. Tan, X. Jiao, H. Ju, Z. Qi, J. Zhu, Y. Xie, Joule 2018, 2, 1004; b) S. Barman, A. Singh, F. A. Rahimi, T. K. Maji, J. Am. Chem. Soc. 2021, 143, 16284; c) X. Li, Y. Sun, J. Xu, Y. Shao, J. Wu, X. Xu, Y. Pan, H. Ju, J. Zhu, Y. Xie, Nat. Energy 2019, 4, 690.
- [23] a) X. Zhu, J. Yang, X. Zhu, J. Yuan, M. Zhou, X. She, Q. Yu, Y. Song, Y. She, Y. Hua, H. Li, H. Xu, Chem. Eng. J. 2021, 422, 129888; b) K. Yan,
- D. Wu, T. Wang, C. Chen, S. Liu, Y. Hu, C. Gao, H. Chen, B. Li, ACS Catal. 2023, 13, 2302; c) L. Liu, Z. Wang, J. Zhang, O. Ruzimuradov, K. Dai, J. Low, Adv. Mater. 2023, 35, 2300643; d) Y. Li, B. Li, D. Zhang, L. Cheng, Q. Xiang, ACS Nano 2020, 14, 10552; e) K. Wang, M. Cheng, F. Xia, N. Cao, F. Zhang, W. Ni, X. Yue, K. Yan, Y. He, Y. Shi, W. Dai, P. Xie, Small 2023, 19, 2207581.
- [24] a) Y. Zhu, L. Yang, J. Ma, Y. Fang, J. Yang, X. Chen, J. Zheng, S. Zhang, W. Chen, C. Pan, B. Zhang, X. Qiu, Z. Luo, J. Wang, Y. Guo, Angew. Chem., Int. Ed. 2023, 62, 202309158; b) Z. Li, G. Zhu, W. Zhang, L. Zhu, B. Cao, J. Gao, X. Shi, Y. Huang, P. Liu, M. Hojamberdiev, Chem. Eng. J. 2023, 452, 139378.
- [25] H. Liu, B. Li, Z. Liu, Z. Liang, H. Chuai, H. Wang, S. N. Lou, Y. Su, S. Zhang, X. Ma, ACS Catal. 2023, 13, 5033.
- [26] L. Wang, T. Yan, R. Song, W. Sun, Y. Dong, J. Guo, Z. Zhang, X. Wang, G. A. Ozin, Angew. Chem., Int. Ed. 2019, 58, 9501.